Supplementary Information

Direct Conversion of Methane to Formic Acid over Au-Fe- Na-ZSM-5 at Ambient Pressure using H_2O_2

Pawan Kumar*[a,b], Iqra Ahangar[c], Srishti Kesarwani[a,b], Rajashri Urkude[d], Nita A. R. Patil[e], Prashant Niphadkar[a], Vijay V Bokade[a,b], M. Ali Haider*[c], C P Vinod*[a,b]

[a] Catalysis and Inorganic Chemistry Division, National Chemical Laboratory (CSIR-NCL), Dr. Homi Bhabha Road, Pune – 411008 (India)

[b] Academy of Scientific and Innovative Research (AcSIR), Ghaziabad-201002, India

[c] Department of Chemical Engineering, Indian Institute of Technology, Delhi, India

[d] BARC Beamlines Section, Raja Ramanna Centre for Advanced Technology, Indore, India

[e] Central NMR Division, CSIR-NCL, Pune – 411008

E-mail: pawankumar.research@gmail.com, cp.vinod@ncl.res.in

This file includes:

Figure S1 to S19

Table S1 to S8

Experimental:

Experimental details of X-ray Absorption spectroscopy

The beamline is equipped with a Si (111) based double crystal monochromator for energy selection and a meridional cylindrical mirror (Rh/Pt coated) for collimation. The data was collected when the synchrotron source 2.5 GeV ring was operated at 120 mA injection current. XAFS (XANES and EXAFS) measurements were carried out at room temperature in fluorescence mode. An ion chamber was filled with N_2, He, and Ar for Fe and Au foil and for the samples. The second crystal of the monochromator was 60% detuned during the data collection to suppress the higher harmonic components. The energy calibration was performed using Fe and Au metal foil as a reference. The standard normalization and background subtraction procedures were executed using the ATHENA software version 0.9.26 to obtain normalized XANES spectra.[1] Fourier transformed (FT) of EXAFS oscillations were calculated to observe the $|\chi(R)|$ vs R space spectra, and its fitting was done using ARTEMIS software version 0.9.26, which uses FEFF6 and ATOMS.[2] programs to simulate the theoretical scattering paths according to the crystallographic structure.

Theoretical Calculations:

Methodology

Fractional coordinates of the MFI zeolite structure were obtained from the Materials Studio 2020 (Biovia, San Diego) database with unit cell parameters: a= 20.022 Å, b = 19.899 Å, c = 13.383 Å and $\alpha = \beta = \gamma = 90°$). From the 96 T sites of the zeolite, two silicon (Si^{4+}) atoms were replaced from the T7 and T12 sites to introduce Aluminium (Al^{3+}) atoms into the framework[3], with charge compensation by the addition of Na^+ positioned in the main 10-membered ring (MR) referred as Na' and the other at a relatively stable position (I2, referred as Na'') connected to the 10 MR ring (Figure 1 a) as suggested by Zhen et al. and Petr Nachtigall et al.[4,5] The proposed active site for methane oxidation consists of a mononuclear iron-oxide and cationic gold (Au^+ZSM-5) species anchored within the MFI framework. [3,6,7] In this, the iron cluster and Au^+ ion are anchored on the framework Al position at T7 and T12, respectively, Figure 1(b). First-principle calculations were

performed using the periodic plane-wave Density Functional Theory (DFT) code available in the Vienna Ab initio Simulation Package (VASP, version 6.2.2).[8,9] The plane wave basis set was expanded to an energy cutoff value of 400 eV, and the exchange-correlation function was described using the Perdew-Burke-Ernzerhof (PBE) functional with generalized gradient approximation (GGA). Core electron potentials are approximated with the projector augmented wave (PAW) pseudopotential.[10,11] For the Fe atom, Hubbard U correction is applied in the DFT+U framework, wherein U-J = 4 was set for Fe as suggested by Rohrbach et al.[12] To account for van der Waals interactions, Grimme DFT-D3 method was implemented.[13] For geometry optimization, force and energy convergence criteria are set at 0.05 eV/Å and 10^{-6} eV, respectively, and a single k-point is employed. All calculations were performed spin polarised with a Gaussian smearing of 0.02 eV. Transition state (TS) structures on the reaction coordinate are identified using the climbing image nudged elastic band (CI-NEB) method[14,15] and applying the same force and energy convergence criteria. Activation energy and reaction energy were calculated as the difference between the TS and initial reactant state structures and the difference between the reactant and product state structures, respectively.

Au (111) surface is modelled with four metal layers and a vacuum of 15 Å in the perpendicular z-direction. Top two layers of the surface model are allowed to relax to mimic the surface relaxation process, while the bottom two are fixed to the bulk lattice coordinates. A Monkhorst-Pack k-point mesh 3x3x1 is used to sample the irreducible Brillouin zone.[16] The rest of the method follows the same parameters of pseudopotential, energy cutoff, force, and energy convergence criteria, and TS search as described for the zeolite structure.

Additionally, we considered Au_{38} nanoparticles as catalytic species to explore their catalytic properties in methane oxidation and activation of hydrogen peroxide.

Current evidence suggests that Fe in ZSM-5 does not predominantly occupy framework positions. Several studies have addressed the local structure of Fe in Fe-ZSM-5. EXAFS and Mössbauer spectroscopic analyses indicate that, following thermal treatment, Fe primarily exists as small, dispersed iron oxide clusters rather than being incorporated into the MFI lattice.[17] In particular, aluminium sites in the zeolite framework play a crucial role in anchoring Fe, thereby stabilising

mononuclear or small oligonuclear Fe species and preventing aggregation.[18] Hutchings and colleagues demonstrated that the dominant product in the H_2O_2-driven oxidation of methane over Fe-based zeolites was formic acid (HCOOH), proposing a mechanistic cycle involving an extra-framework diiron active site.[19] Various spectroscopic and computational investigations, including DFT simulations, have confirmed that the di-iron species $[Fe_2(\mu_2\text{-}OH)_2(OH)_2(H_2O)_2]^{2+}$ acts as a key catalytic centre in Fe/ZSM-5 for methane oxidation.[20–22] Further literature supports the role of extra-framework Fe in forming the reactive α-oxygen species, with some studies linking mononuclear Fe to higher methanol productivity, while others emphasise di-iron species as key catalytic centres, particularly when N_2O is used as an oxidant.[23,24] Based on existing literature[25] and our characterization results, we confirm that Fe is not incorporated into the MFI framework of Na-ZSM-5. Instead, it exists as an extra-framework species, likely residing on the external surface or within the pores of the zeolite. Given the low Fe loading (<0.5 wt%), framework substitution is highly unlikely. This conclusion is supported by electron microscopy, elemental mapping, and X-ray absorption spectroscopy (XAS), all of which indicate the presence of well-dispersed Fe species outside the zeolite framework.

The anchoring of Au within ZSM-5 remains more complex. Multiple models have been proposed to describe Au species in zeolite environments. Graham Hutchings and others have investigated Au^+ cations stabilised in the 10-membered ring channels of ZSM-5 (Au^+/ZSM-5), as well as Au_{38} nanoparticles and Au(111) slab models to study methane oxidation mechanisms.[26] Similar systems have also been explored through DFT calculations to understand the mechanistic pathways involved. While current evidence suggests skeletal Fe incorporation is unlikely, our spectroscopic evidence (electron microscopy, XAS and XPS) supports the electronic interaction and close vicinity of Au and Fe. So it suggests that anchoring of Au is predominantly facilitated by these non-framework Fe species, rather than by any Fe incorporated into the zeolite framework.

Synthesis: Synthesis of NZ

Na-ZSM-5 was prepared using a molar gel composition: SiO_2/0.0125Al_2O_3/0.3Na_2O/0.1TPABr /36 H_2O. Typically, 7.86 g of TPABr and 30.0 g of DI water were dissolved with stirring to produce Solution A. Solution B was prepared separately by mixing 62.60 g sodium silicate (28% SiO_2 & 8% Na_2O) in 30.0 g water with vigorous stirring. Then, solution B was slowly added to solution A, referred to as solution C. 2.43 g of aluminum sulfate was carefully mixed in an acidic solution containing 5.13 g of Sulfuric acid and 10.0g of water. This alumina solution (solution D) was then slowly added to solutions C and E, with vigorous stirring for 2h. Finally, 69.5 g of water was added to solution E with stirring for 1 h to produce a final gel, and the pH was maintained at 10.0 $\pm$0.2. The final gel was transferred to an SS autoclave and subjected to hydrothermal crystallization at 160 °C for 48 h. After hydrothermal crystallization, the gel was separated into a wet cake by vacuum filtration, then dried at 120 °C and calcined in a muffle furnace at 550 °C for 10 h to obtain a ZSM-5 composite in Na-form.

Synthesis of FeNZ catalyst

Iron (Fe) was deposited over NZ using the well-known deposition precipitation method. Typically, 0.5 grams of NZ were dispersed in 50 mL of Millipore water with sonication for 5 to 10 minutes. For metal deposition over the support, the pH of the solution was adjusted to 9.5 using a 0.1 M NaOH solution while stirring (rpm 400). Then, the 25mL of aqueous solution, in a burette, containing the metal precursor (Note: amount of the precursor is taken according to the theoretical weight loading) was slowly added drop by drop to the above solution for 20 to 30 minutes, maintaining the pH at 9.5. The mixture was then aged for 1 h, followed by centrifugation and washing with deionized water twice. After centrifugation and drying in a hot air oven at 80 °C for 12 h, a solid powder was obtained. This powder was calcined in static air at 350 °C for 4 h (Ramp rate- 2°C/min). The resulting powder catalyst (xFeNZ, x = wt% of Fe) was utilized for catalytic reactions without undergoing additional post-treatment.

Synthesis of AuFeNZ catalyst

Deposition of Au onto the FeNZ catalyst was also carried out using the deposition-precipitation method. Typically, 0.5 grams of FeNZ catalyst were dispersed in 50 mL of Millipore water with sonication for 5-10 minutes, and 2 mmol of ammonium chloride was introduced into the solution as a modifier under stirring (rpm 400). Subsequently, with the help of a burette, 25 mL of aqueous solution containing the Au precursor (Note: amount of the precursor is taken according to the theoretical weight loading) was slowly added dropwise to the resulting solution while maintaining the pH at 9.5 with a 0.1M aqueous NaOH solution. The resulting precipitate was centrifuged, washed with deionized water, and dried at 80 °C for 12 h. The dried powder was further calcined in static air at 350 °C for 4 h (Ramp rate- 2°C/min), yielding the resulting powder catalyst (yAuxFeNZ, y = wt% of Au), which was utilized for catalytic reactions without any additional post-treatment. For the synthesis of AuNZ, NZ support was used in place of FeNZ, keeping all the other steps constant.

Product Quantification:

Product quantification using NMR:

The solution consisted of liquid products filtered from the catalyst powder using centrifugation. The clean liquid, containing products including acetic acid, methanol, formic acid, methyl peroxide, and others, was quantitatively analyzed using ^{1}H-NMR. KHP dissolved in a mixture of D_2O and H_2O was used as a calibration standard. The analysis of methane conversion into various liquid products was conducted using proton nuclear magnetic resonance (^{1}H NMR) spectroscopy (AV-NEO400, Bruker BioSpin AG; Magnet system 400MHz). Following the reaction, 0.5 mL of the reaction mixture was combined with 0.08 mL of deuterium oxide and 0.02 mL of potassium hydrogen phthalate (KHP) stock solution, serving as the internal standard (at a concentration of 1 mM) in an NMR tube. The concentration of the liquid products generated in the catalytic experiments was determined using the following formula.[27]

$$\frac{n_x}{n_y} = \frac{I_x}{I_y} \times \frac{N_y}{N_x}$$

In this context, n_x denotes the molar concentration of KHP, while I_x refers to the integral area observed in the ^{1}H NMR spectra for KHP. Additionally, N_x represents the number of nuclei, corresponding to the four equivalent protons of KHP that appear at 7.25 ppm. Likewise, n_y is derived using the same formula for the liquid product. I_y indicates the integral area of the resulting product, and N_y signifies the number of nuclei linked to the respective peak. During the NMR measurements, a solvent suppression program was run to minimize the signal originating from H_2O. Each catalysis experiment generated a 20 mL solution of left H_2O_2 and liquid products (methanol, formic acid, methyl peroxide, acetic acid). Ratios of peak areas of methanol, formic acid, or methyl peroxide to the peak area of KHP were calculated.

Product quantification using GC:

Liquid products were analyzed using a GC (NUCON-5765) equipped with a DB-624 column using a split mode with a flame ionization detector (FID). The chromatographic conditions were: helium as the carrier gas at a flow rate of 2 mL/min, injection volume: 1 µL, inlet temp: 200 °C, detector temperature was set at 240 °C, column oven temperature was initially at 60 °C for 6 min, then increased up to 200 °C at 10 °C/min. Products were quantified using a calibration plot of the liquid products using an area under the curve method.

Note: The DB-624 stationary phase is optimized for volatile organic compounds and residual solvents, whereas formic acid is highly polar, corrosive, and exhibits strong adsorption on both the injector and the column, leading to severe peak distortion and poor sensitivity. Due to these limitations, GC analysis was not suitable for formic acid. Therefore, formic acid was quantified by ^{1}H NMR spectroscopy, which provided accurate and reproducible measurements in the presence of methanol

The gases after catalysis are analyzed with a GC (NUCON-5765) equipped with a methanizer unit with FID with a Carboseive column. The chromatographic conditions were: helium as the carrier gas at a flow rate of 2 mL/min, injection volume: 100 µL, detector temperature was set at 240 °C, column oven temperature was at 90 °C. Retention times for CO, CH_4 and CO_2 were 2.8 minutes, 4.8 minutes and 8.9 minutes, respectively. The amount of CH_4, CO and CO_2 after the catalysis was

calculated by using the standard calibration for the same. After the analysis, the area under the curve was measured and calculated.

For sample collection during the batch process, the reactor was initially cooled to below 10 °C. The gas was collected in a balloon using the gas valve and then manually injected into the gas chromatograph (GC) at ambient temperature and pressure with an airtight syringe. For the liquid samples, the liquid was extracted from the reactor and centrifuged prior to injection into the GC.

In the continuous flow process, the liquid samples were also cooled to below 10 °C, followed by centrifugation and GC injection at various time intervals. For the gas samples, an airtight syringe was used to collect samples from the outlet tubing of the reactor.

Centrifugation was performed to ensure that no solid particles were introduced into the GC column.

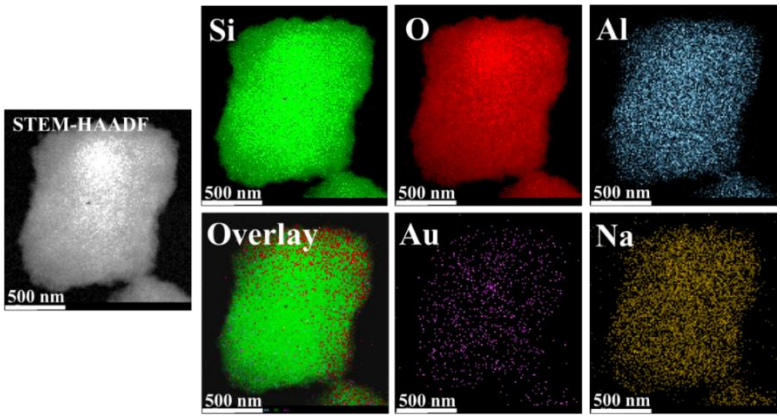

Figure S1. TEM-EDX mapping of 0.1AuNZ.

This analysis reveals the uniform distribution of all elements over the surface of the zeolite.

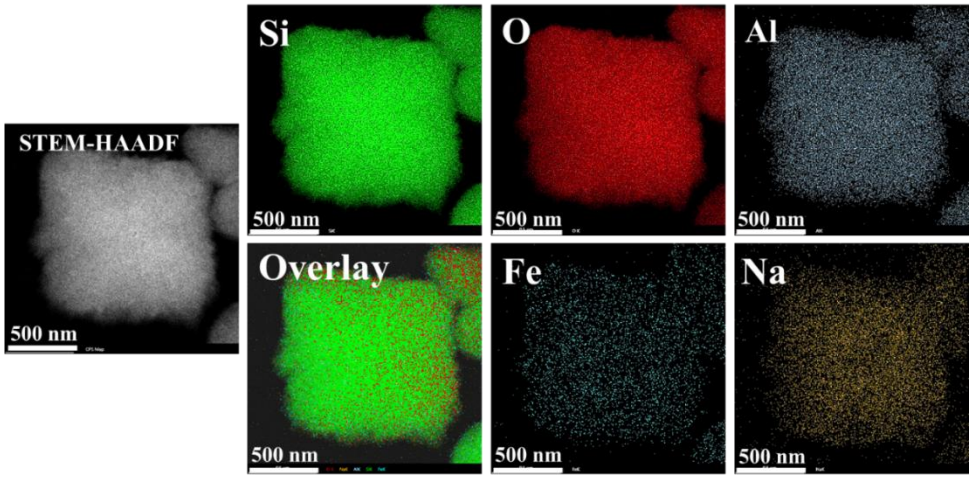

Figure S2. TEM-EDX mapping of 0.1FeNZ.

This analysis reveals the homogeneous distribution of all elements over the surface of the zeolite.

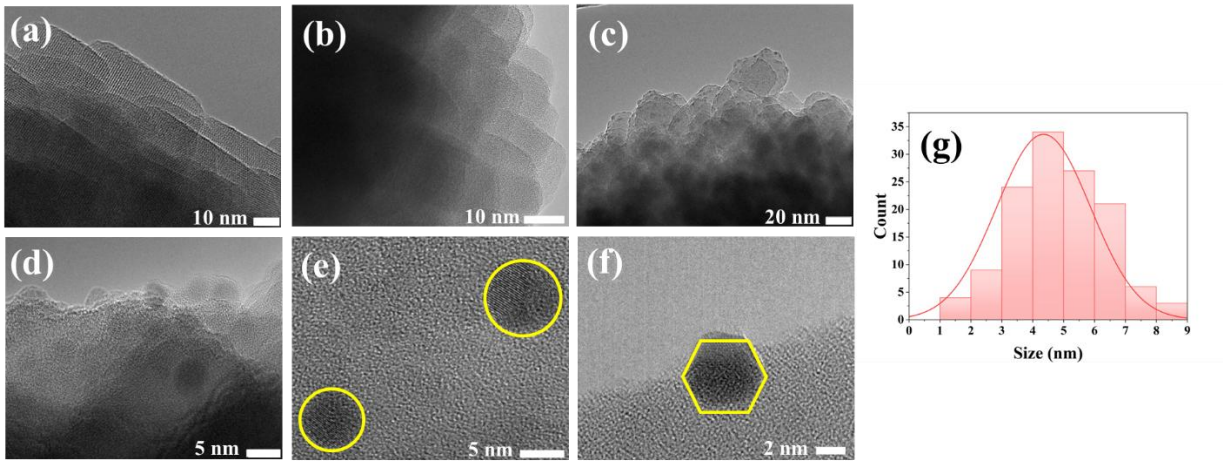

Figure S3. High-resolution TEM images of (a) NZ, (b) 0.1FeNZ, (c-f) 0.1Au0.1FeNZ and (g) particle size distribution histogram of 0.1Au0.1FeNZ (HRTEM).

In the case of NZ (Figure S3a), lattice fringes of zeolite can be seen in ordered crystalline zeolite. In the TEM image of 0.1FeNZ (Figure S3b), no Fe particles were seen because of the single atomic nature of the Fe, as confirmed by XAS analysis. While for AuFeNZ (Figure S3b), the analysis confirms the presence of spherical and hexagonal Au particles over the FeNZ catalyst. The d spacing of 0.2 nm confirms the Au(111) phase. The high-contrast spots observed in the STEM images are attributed to Au due to the significantly higher atomic number and scattering contrast of Au compared to Fe. Au atoms/nanoparticles appear considerably brighter in HAADF-STEM imaging due to Z-contrast, which makes it possible to distinguish them from Fe species. Furthermore, the observed particles are 2–3 nm in size, which is consistent with Au nanoparticles and not with the atomically dispersed Fe species used in this study. The absence of lattice fringes of the zeolite in the metal-supported catalyst may be due to contrast masking and deposition-induced disorder.

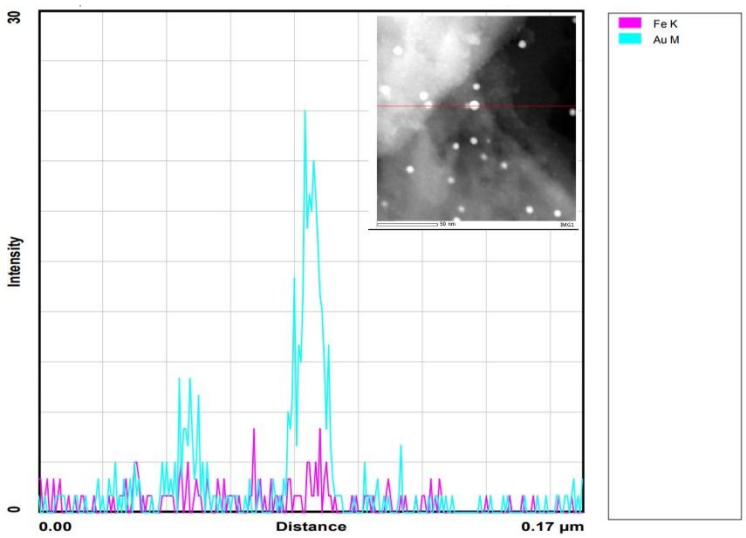

Figure S4. STEM line analysis of 0.1Au0.1FeNZ.

This analysis reveals the interaction between Au and Fe decorated over NZ. Wherever the Au signal grows at the same place, iron presence can be observed, confirming the close proximity of Au and Fe which results in direct interaction and, hence reactivity

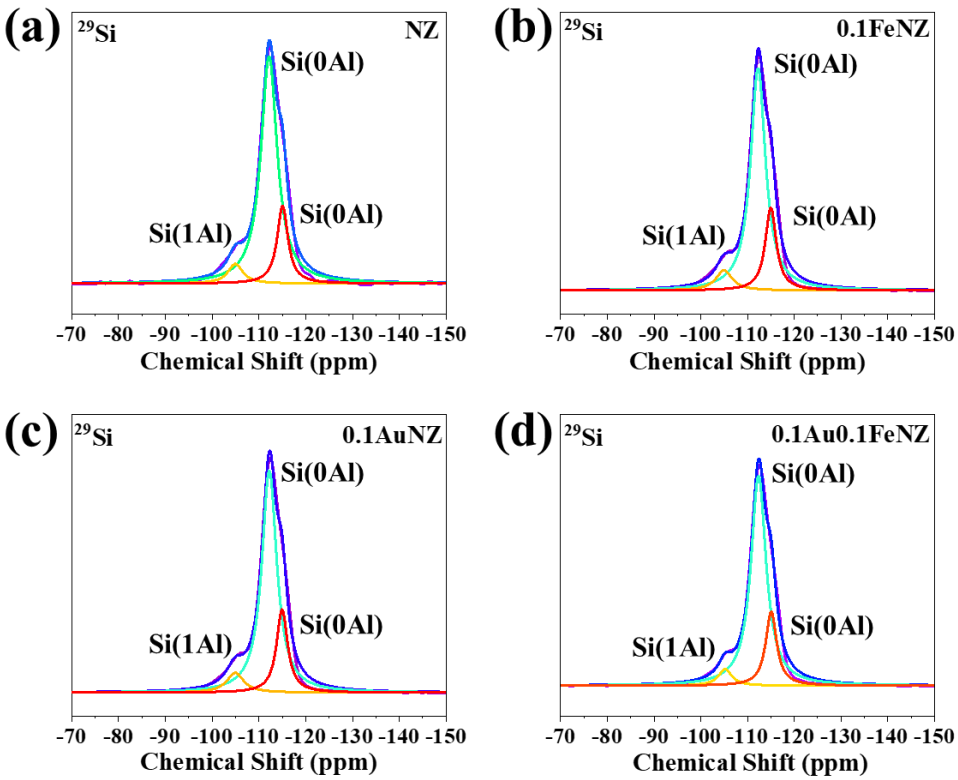

Figure S5. ^{29}Si MAS NMR spectrum of various catalysts.

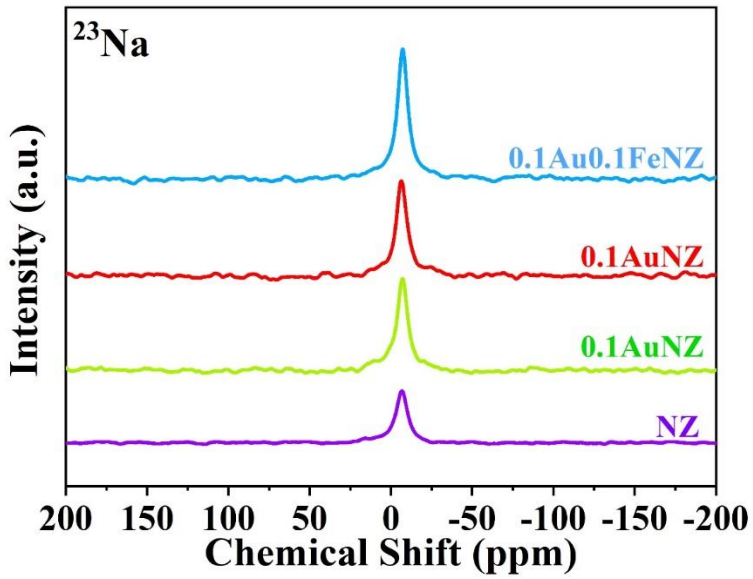

Figure S6. ^{23}Na MAS NMR spectrum of various catalysts.

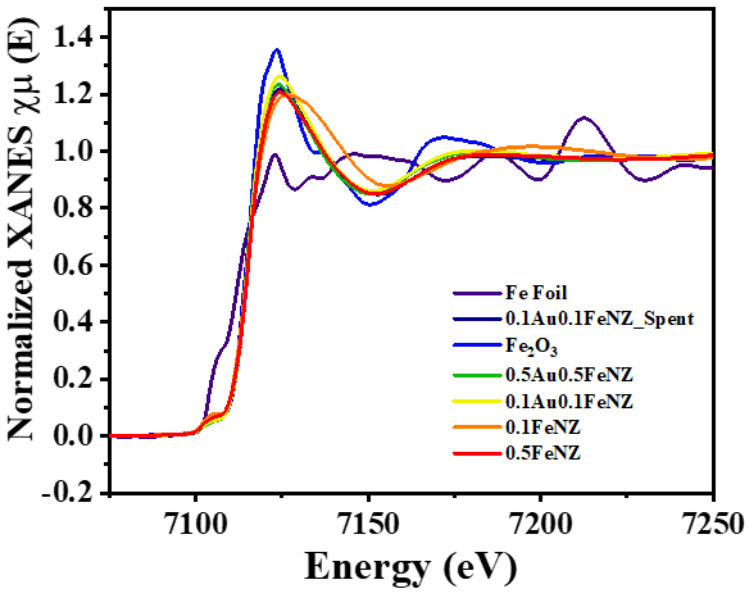

Figure S7. Normalized XANES spectra measured at Fe K-edge and Fe standards

.

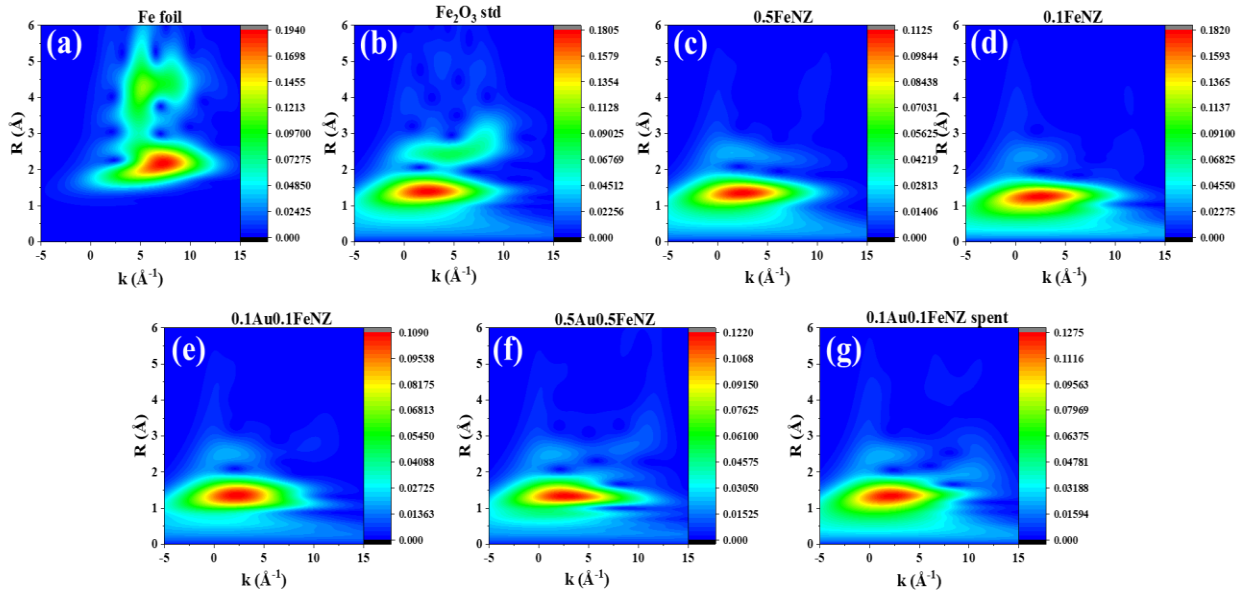

Figure S8. Wavelet transformed EXAFS spectra measured at Fe K-edge and Fe standards.

In the Fe K-edge EXAFS, although no distinct Au–Fe scattering paths were observed, changes in the wavelet transform features may be attributed to the presence of nearby Au species. And there are high chances of the merging of the Au-Fe feature in the contour area Fe-O scattering feature because of the similar radial distance of the two. Therefore, we propose the interaction to be of the Au–O–Fe type, rather than a direct Au–Fe bond.

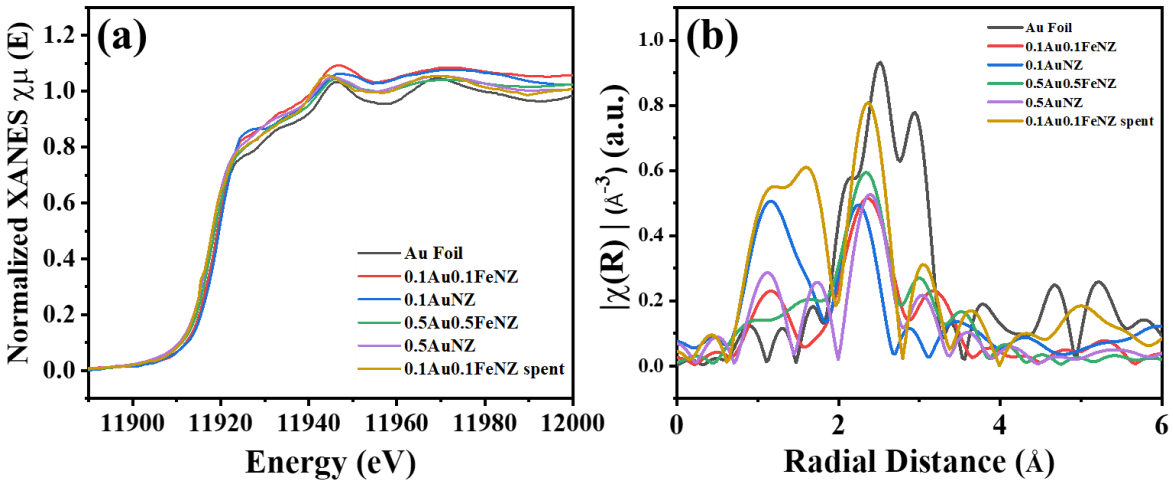

Figure S9. (a) Normalized XANES spectra at Au L_3-edge of various catalysts, (b) FT of EXAFS spectra χ(R) vs. R data of Au-Fe catalyst measured at Au L_3-edge.

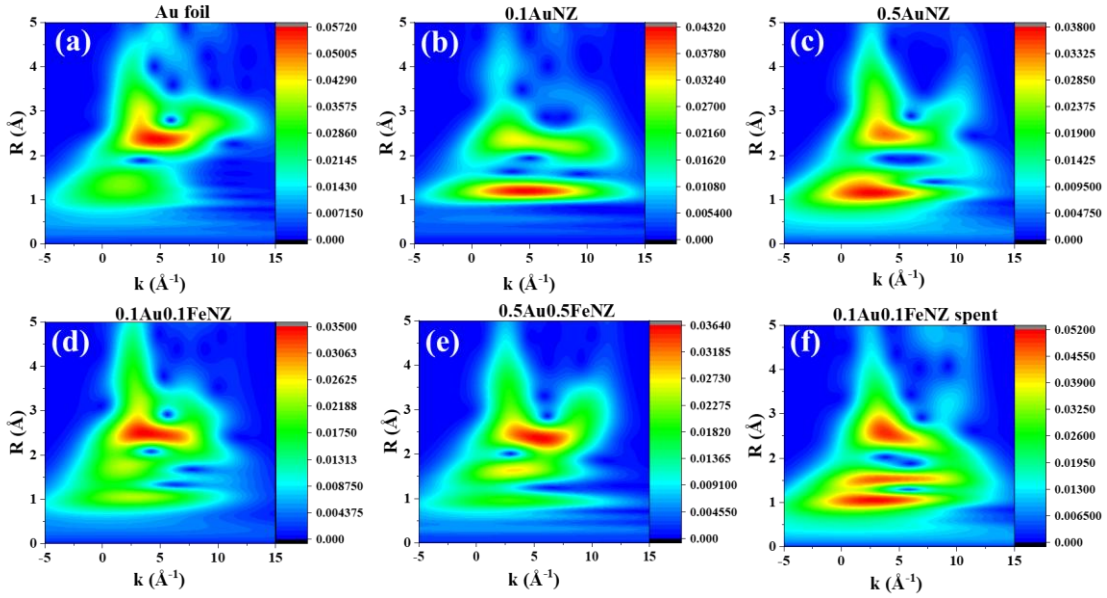

Figure S10. Wavelet transformed EXAFS spectra measured at Au L_3-edge and Au standards.

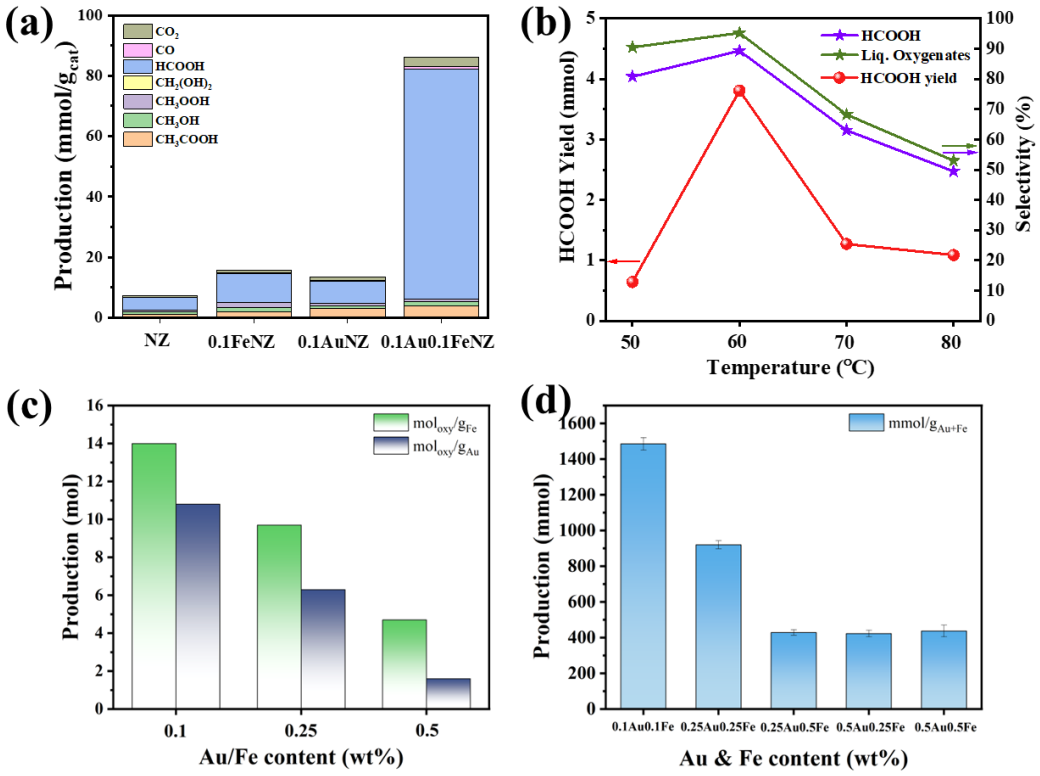

Figure S11. (a) Catalytic activity of various catalysts, (b) catalytic activity of 0.1Au0.1FeNZ at different reaction temperatures, (c &d) catalytic activity with different Au/Fe and Au+Fe content, respectively. Reaction conditions: 50 mg Catalyst, 0.5 h, 10 bar Methane, 980 rpm, 20 mL 5M H_2O_2 (a-c) and 0.25M H_2O_2 (d).

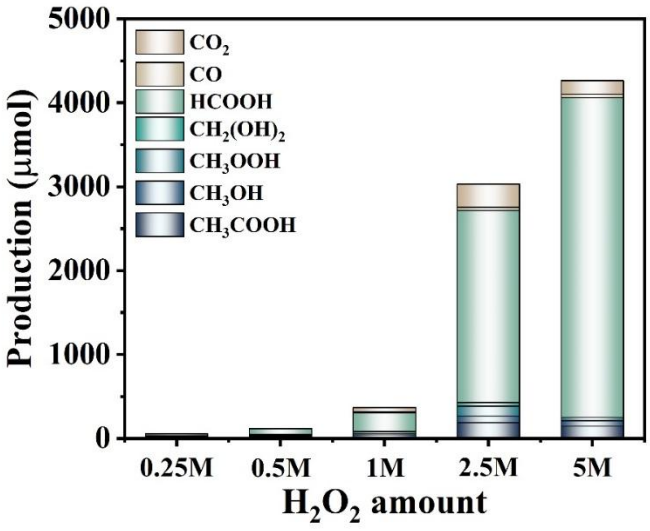

Figure S12. Catalytic activity of 0.1Au0.1FeNZ at different amounts of oxidant. Reaction conditions: 50 mg Catalyst, 60 °C, 0.5 h, 10 bar Methane, 980 rpm.

This analysis shows that the productivity of the catalysts is directly proportional to the amount of the oxidant provided in the reaction, and the utilization efficiency of H_2O_2 for the 0.1Au0.1FeNZ catalyst is around 4.6 % for the batch process in 5M H_2O_2. The efficiency is calculated using the initial amount of the H_2O_2 and the production of oxygenates.

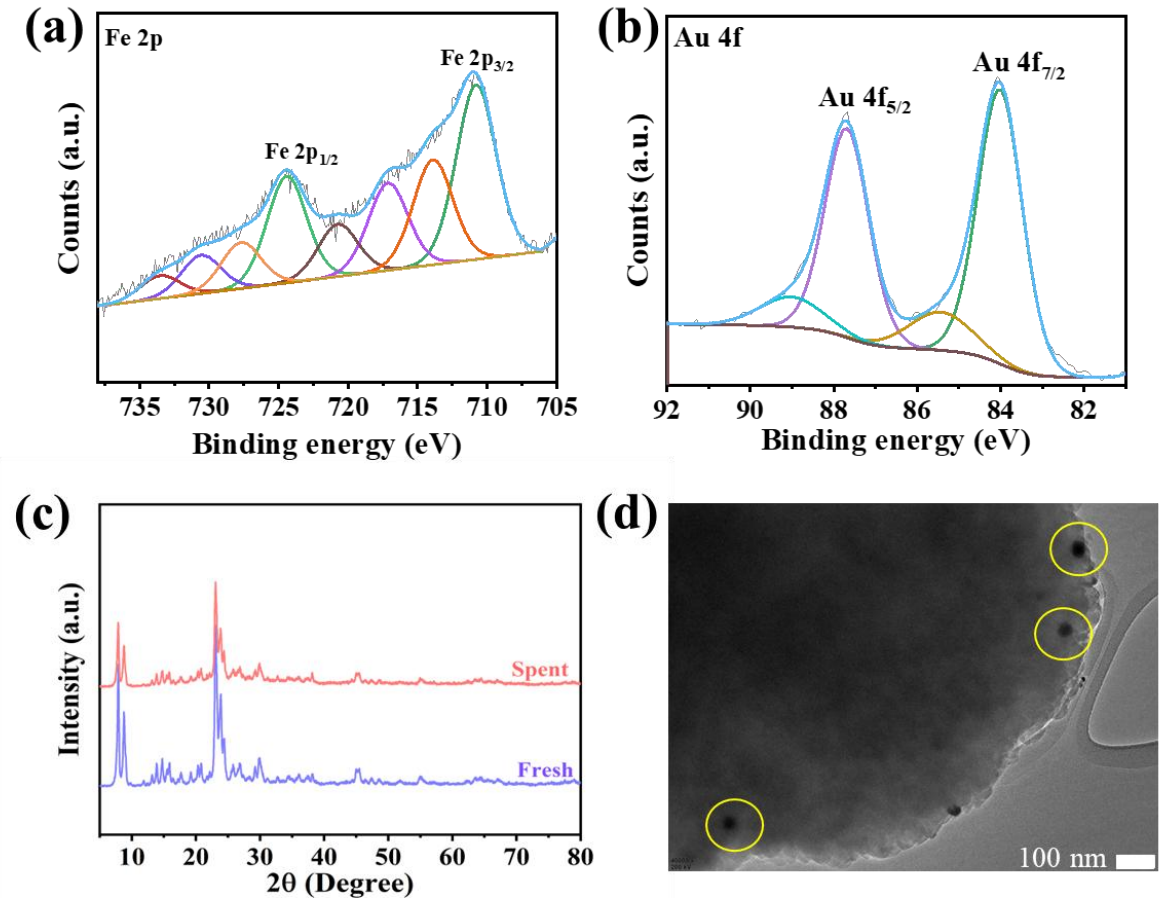

Fig. S13. (a and b) Fe 2p and Au 4f XPS spectra of spent catalyst, respectively, (b) XRD spectra of fresh and spent catalyst, and (d) HRTEM image of spent catalyst. [Note: the spent catalyst (0.1Au0.1FeNZ) was analyzed after a 13h continuous flow reaction.

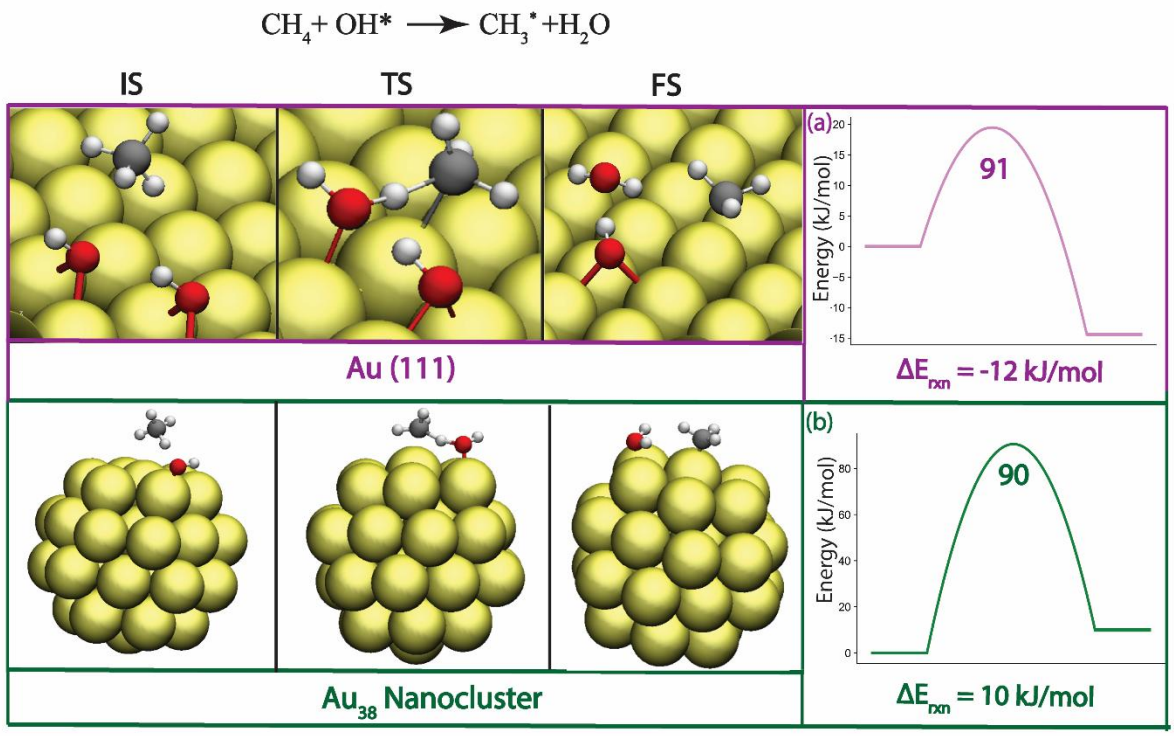

Figure S14. The DFT-simulated pathway over the (a) Au (111) and (b) Au_{38} nanoparticle for the C-H bond activation in methane to CH_3 radical.

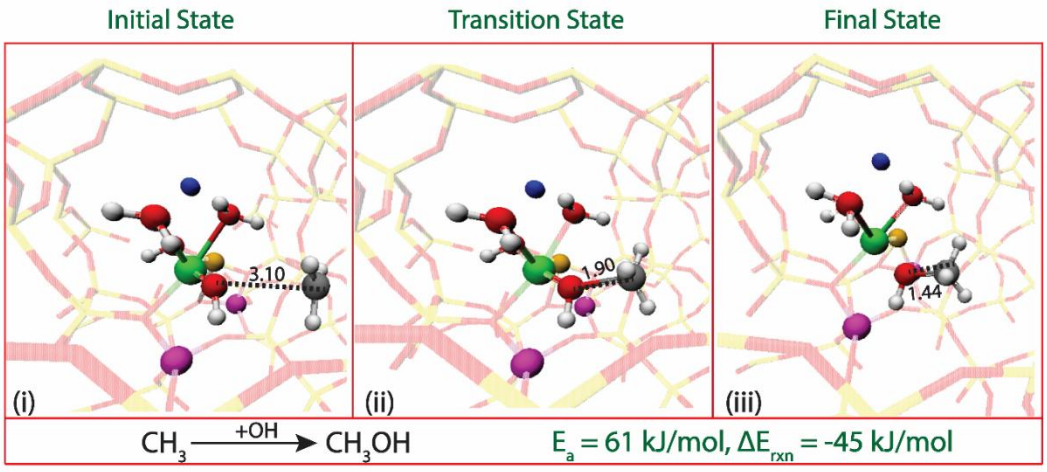

Figure S15. The DFT-simulated pathway for methanol formation in the AuFeNZ catalyst.

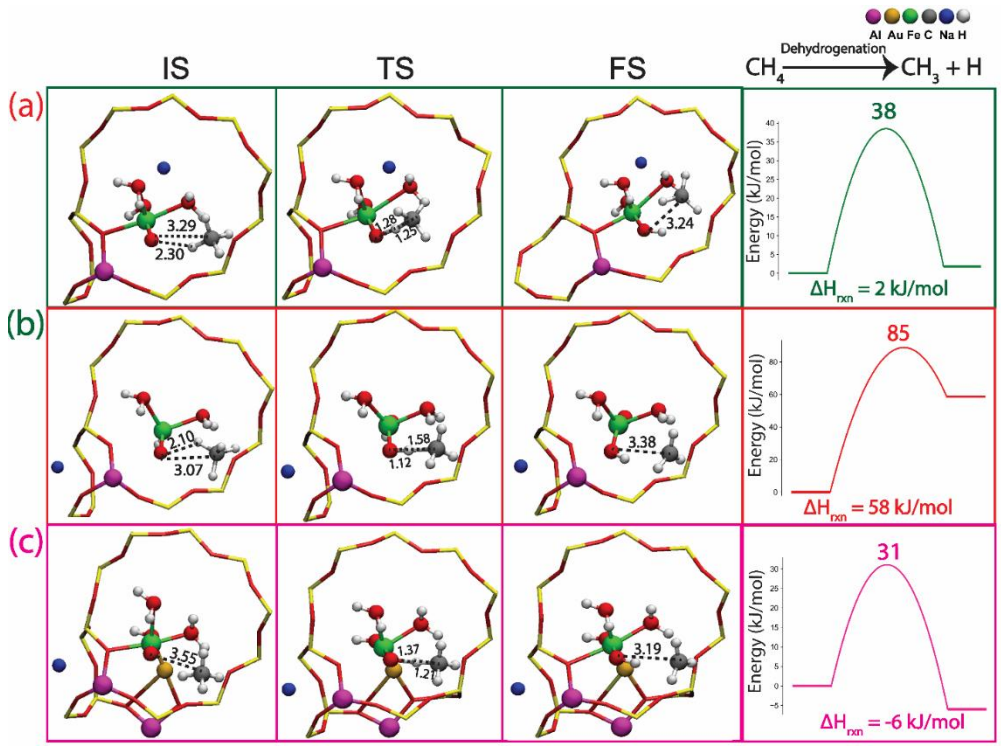

Figure S16. The DFT-simulated calculation for the C-H bond activation of the CH_4 over the mononuclear Fe species anchored in zeolite (a) The optimized initial state (IS), transition state (TS) and final state (FS) for methane activation in Fe Na'-ZSM-5 (b) within zeolite framework of Fe Na''-ZSM-5 (c) within zeolite Au/Fe Na''-ZSM-5. For clarity, only the active sites and the zeolite ring are depicted.

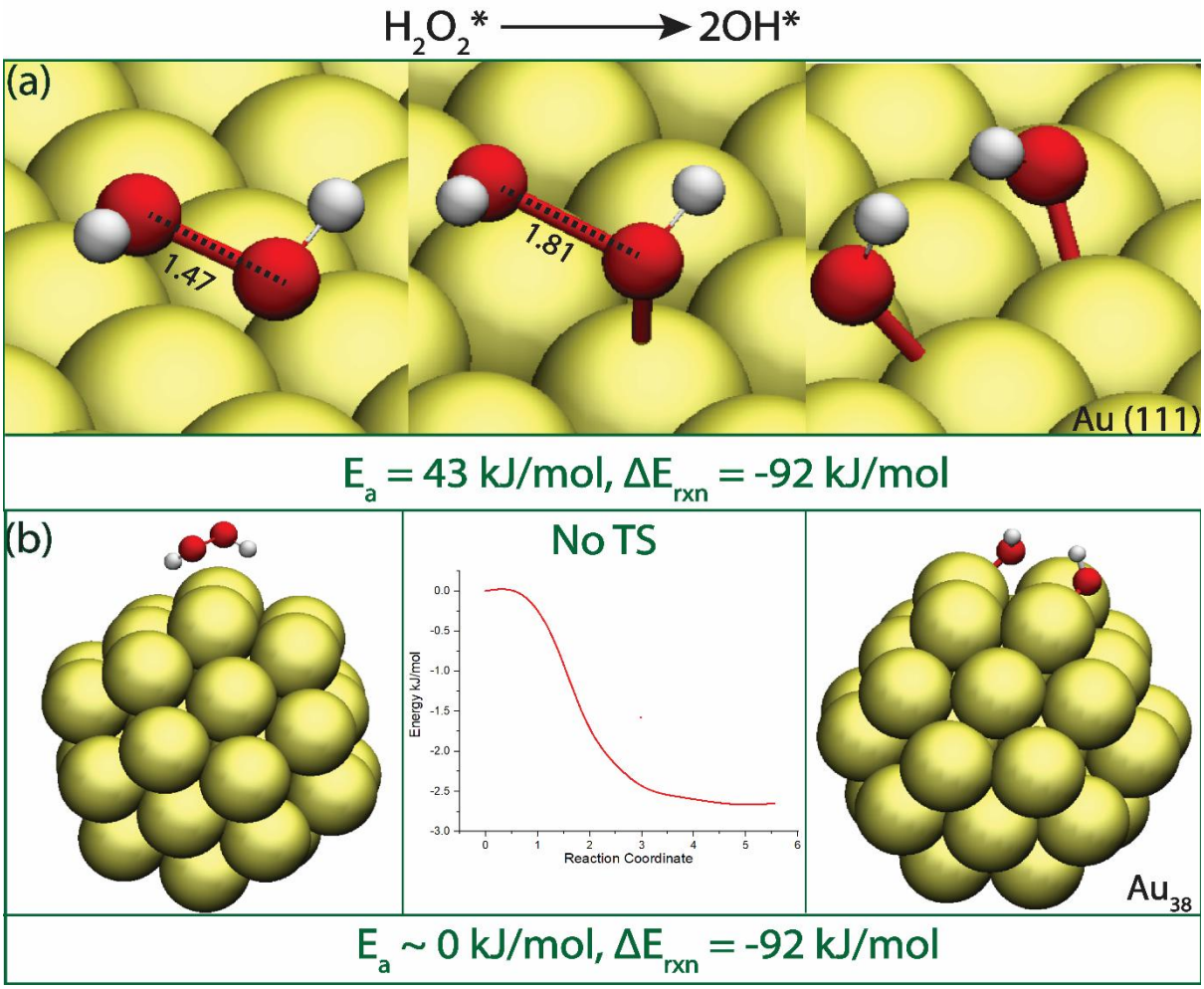

Figure S17. The DFT-simulated calculation for the H_2O_2 dissociation into OH radicals (a) The optimized initial state (IS), transition state (TS) and final state (FS) over the slab Au (111) (b) Radical (OH) formation Au_{38} nanoparticle.

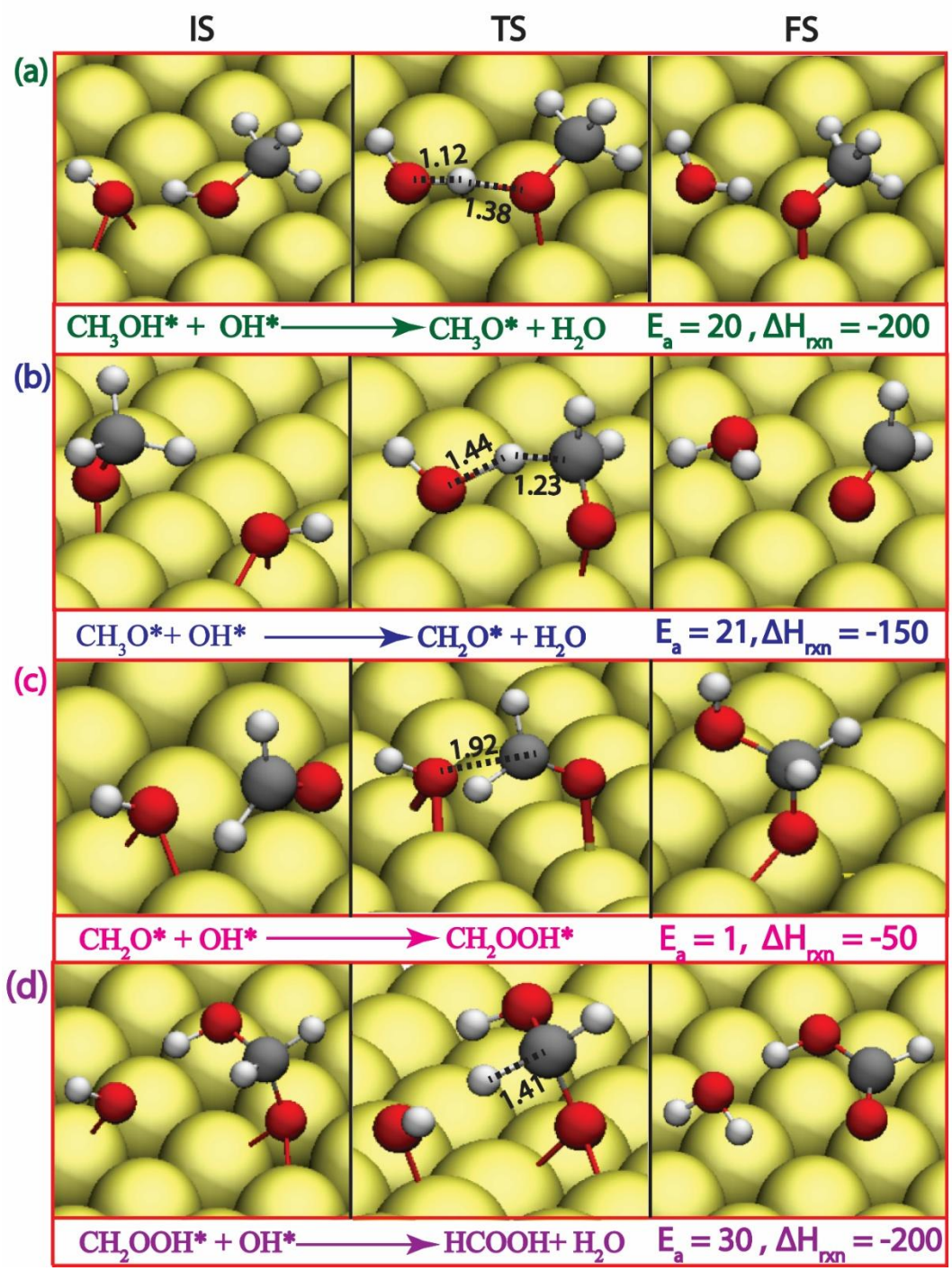

Figure S18. (**a-d**) The DFT-simulated pathway over the Au (111) for the oxidation of CH_3OH to HCOOH using H_2O_2 as the oxidant. For clarity, only the top layer of metal is depicted.

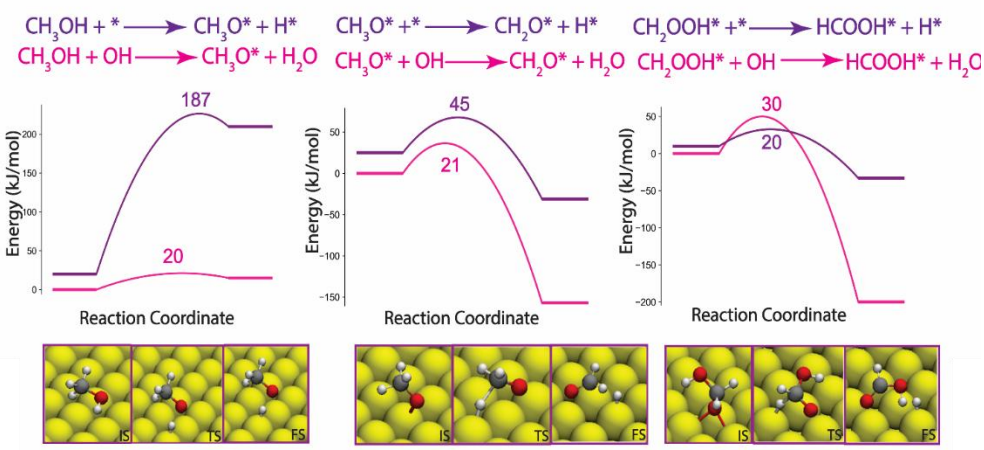

Figure S19. The comparison DFT-simulated pathway over the Au (111) and surface-bound hydroxide intermediates for the (a) C-H bond activation of CH_3OH to alkoxy intermediate, (b) activation of C-H bond in alkoxy intermediate to HCHO and (c) C-H bond cleavage in CH_2OOH to form HCOOH.

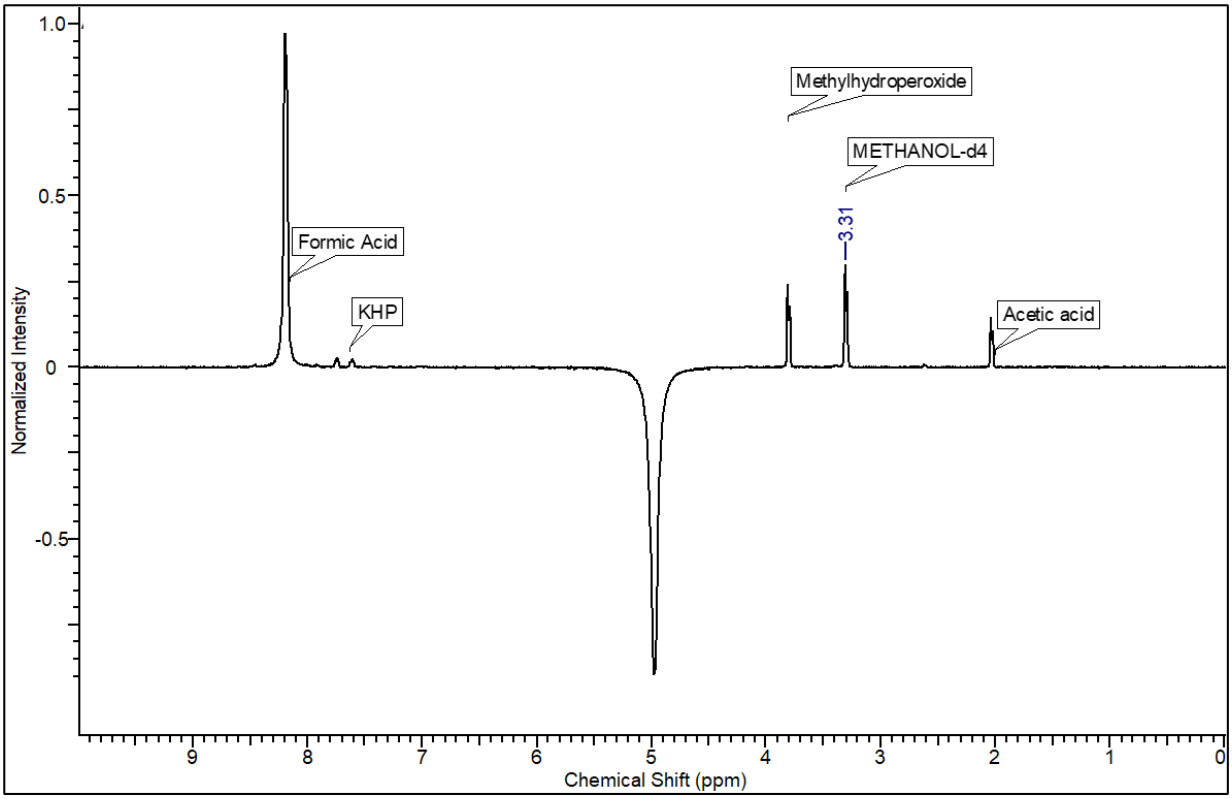

Figure S20. ^{1}H NMR profile of reaction mixture in H_2O+D_2O (NMR solvent) using KHP as internal standard. Reaction conditions: 50 mg 0.1Au0.1FeNZ catalyst. 0.5 h, 60 °C, 5 M H_2O_2 (20 mL).

Chemical Shift (ppm): 2.0 (Acetic acid), 3.3 (Methanol), 3.8 (Methyl-hydroperoxide), 7.6 (KHP) and 8.3 (Formic acid)

Table S1. ICP-OES analysis of various catalysts.

Sr. No.	Catalyst	Fe Loading (wt%)	Au Loading (wt%)
1	NZ	-	-
2	0.1FeNZ	0.092	-
3	0.1AuNZ	-	0.089
4	0.1Au0.1FeNZ	0.093	0.089
5	0.5Au0.5FeNZ	0.046	0.043

Table S2. N_2 sorption analysis data of various catalysts

Sr. No.	Catalyst	Specific Surface Area (m^2/g)	Pore volume (cc/g)	Pore diameter (nm)
1	NZ	330	0.2	1.5
2	0.1FeNZ	335	0.2	1.5
3	0.1AuNZ	327	0.2	1.5
4	0.1Au0.1FeNZ	339	0.2	1.5

Table S3. EXAFS fitting parameters for Fe K-edge.

Sample	**Bond**	**N**	**R (Å)**	**σ^2**	**ΔE_0**	**R-factor**
0.1FNZ	Fe-O_1	6	1.840 +/- 0.011	0.003 +/- 0.002	-1.783 +/- 1.206	0.016
	Fe-Fe	6	3.117 +/- 0.138	0.035 +/- 0.027		
	Fe-O_2	6	3.467 +/- 0.027	0.003 +/- 0.002		
0.5FNZ	Fe-O_1	6	1.933 +/- 0.017	0.003 +/- 0.004	-3.785 +/- 1.614	0.021
	Fe-Fe	6	2.913 +/- 0.031	0.011 +/- 0.005		
	Fe-O_2	6	3.559 +/- 0.017	0.003 +/- 0.004		
0.1Au0.1FeNZ	Fe-O_1	6	1.980 +/- 0.020	0.019 +/- 0.004	-1.749 +/- 1.521	0.017
	Fe-Fe	6	3.006 +/- 0.082	0.063 +/- 0.018		
	Fe-O_2	6	3.625 +/- 0.082	0.063 +/- 0.018		
0.5Au0.5FeNZ	Fe-O_1	6	1.875 +/- 0.010	0.004 +/- 0.002	-9.012 +/- 1.280	0.010
	Fe-Fe	6	2.937 +/- 0.028	0.005 +/- 0.004		
	Fe-O_2	6	2.596 +/- 0.021	0.007 +/- 0.002		
0.1Au0.1FeNZ spent	Fe-O_1	6	1.995 +/- 0.018	0.017 +/- 0.004	2.237 +/- 1.310	0.018
	Fe-Fe	6	3.102 +/- 0.048	0.035 +/- 0.008		
	Fe-O_2	6	3.850 +/- 0.634	0.132 +/- 0.183		

N: coordination number; *R*: bond distance; σ^2: Debye-Waller factor; ΔE_0: the inner potential correction. *R* factor: goodness of fit.

Note: The Fe-Fe feature accounts for less than 5% of the total Fe species. While minimal, we chose to retain it in the fitting data to ensure full transparency and clarity for readers.

Table S4. Catalytic activity of various catalysts with different loadings of Au and Fe over NZ in the batch process.

Sr. No.	Catalyst	Products (µmol)								HCOOH Sel. (%)
		CH_3COOH	CH_3OH	CH_3OOH	$CH_2(OH)_2$	HCOOH	CO	CO_2	Total	
1	NZ	2.1	2.3	3.2	4	23	2.5	3.3	40.4	56.9
2	0.1Au0.1FeNZ	7.3	6.5	7.4	11.1	105.8	2.3	8.1	148.5	71.2
3	0.25Au0.25FeNZ	25.3	13.7	7.1	15.9	154.8	2.5	11.2	230.5	67.2
4	0.25Au0.5FeNZ	14.3	11.5	3.9	5.8	65.2	7.1	53.1	160.9	40.5
5	0.5Au0.25FeNZ	11.7	11.0	3.8	20.1	95.1	2.8	14.4	158.9	59.9
6	0.5Au0.5FeNZ	12.9	12.2	3.5	13	121	8.7	47.4	218.7	55.3
7	0.1Au0.1FeHZSM	2.7	2.2	1.9	4.1	28.0	1.8	21.6	62.3	44.9
8	0.1AuHZSM	1.8	2.1	1.8	2.8	13.1	1.3	8.3	31.2	42.0
9	0.1FeHZSM	2.6	2.5	2.9	3.1	21.1	1.8	10.3	44.3	47.6

Reaction conditions: 50 mg Catalyst, 0.25 M H_2O_2 (20 mL), 60 °C, 0.5 h, 10 bar Methane, 980 rpm.

Table S5. The catalytic activity of various catalysts in a batch process.

Sr. No.	Catalyst	Products (µmol)								HCOOH Sel. (%)	Oxy. (mmol/g_{cat})
		CH_3COOH	CH_3OH	CH_3OOH	$CH_2(OH)_2$	HCOOH	CO	CO_2	Total		
1	NZ	19.0	45.0	35.1	0	200.2	5.2	27.3	331.8	60.4	6.6
2	0.1FeNZ	32.2	72.1	74.8	0	469.4	17.3	35.4	701.2	66.9	14.0
3	0.1AuNZ	18.2	48.1	38.7	3.9	365.6	12.8	54.6	541.9	67.5	10.8
4	0.1Au0.1FeNZ	147.0	63.2	42.0	0	3808.8	44.0	159.0	4264.0	89.3	85.3
5	0.1AuNZ + 0.1 FeNZ	14.3	52.1	43.6	0	376.8	13.3	38.9	539.0	69.9	10.6
6	0.25FeNZ	65.1	131.2	118.3	0	793.8	32.1	70.1	1210.6	65.5	24.2
7	0.5FeNZ	73.7	126.5	123.2	6.9	692.2	28.3	129.6	1180.4	58.6	23.6
8	0.25AuNZ	30.3	62.8	53.3	5.7	530.1	18.1	98.2	798.5	66.4	15.97
9	0.5AuNZ	33.2	61.2	54.6	5.3	518.6	21.2	123.8	817.9	63.4	16.34

Reaction conditions: 50 mg Catalyst, 5 M H_2O_2 (20 mL), 60 °C, 0.5 h, 10 bar Methane, 980 rpm.

Table S6. Controlled experiments for catalytic activity in batch process.

Sr. No.	Catalyst	Reaction feed	Products (µmol)
1	0.1Au0.1FeNZ	$CH_4 + H_2O_2$	4264.0
2	0.1Au0.1FeNZ	$N_2 + H_2O_2$	0
3	0.1Au0.1FeNZ	CH_4 + No oxidant	0
4	No Catalyst	$CH_4 + H_2O_2$	0

Reaction conditions: 50 mg Catalyst, 5M H_2O_2 (20 mL), 60 °C, 0.5 h, 10 bar Methane, 980 rpm.

Table S7. Catalytic activity comparison with the existing literature.

Catalyst	Selectivity (%)		Product amounts (µmol)					Reaction conditions				Ref.
	Oxy.	HCOOH	CH_3OH	CH_3OOH	HCOOH	CO_2	Oxy.	t (h)	P (bar)	T (°C)	H_2O_2 (M)	
Pd_1O_4/ZSM-5	96.2	56	7.39	39.4	60.8	4.2	107.6	0.5	30	50	0.5	28
	87.9	96	10.9	1.74	338.4	48.2	351.1	0.5	30	95	0.5	
Fe/MOR	~91	~20	~40	~25	~100	~25	~240	1	30	50	0.5	29
	~88	~80	~25	~5	~250	~40	~280	1		100		
0.03wt.% Fe/ZSM-5(66)	94	86	295	83	3832	268	4210	0.5	30	80	5	30
	95.1	84.4	6.9	51.1	457	26.4	515	0.5	30	80	0.5	
Fe-ZIF-8-0.28	96.8	96.8	0.1	1.0	32.6	-	33.7	0.5	30	50	0.5	31
0.1Au0.1FeNZ	95.2	89.3	63.2	42	3808	159	4264	0.5	10	60	5	**This Work**
0.1Au0.1FeNZ	97	79	1	1.2	18.8	-	21	9	1	80	8.5	**This Work**

Table S8. Green Chemistry Metrics

Metric	Value	Notes
Methane charged	35.5 mmol	10 bar at 25 °C, 88 mL gas volume
H_2O_2 used	100 mmol	5 M, 20 mL aqueous
Products	4.2 mmol	Main product (90% selectivity)
Carbon efficiency	10.8%	(4.2 / 35.5) × 100
Atom economy	92%	Based on $CH_4 + H_2O_2 \rightarrow HCOOH$
Reaction mass efficiency	4.6%	Product mass / total reactants
E-factor	21.4	Waste mass/product mass
CO_2 selectivity	4–5%	Minor overoxidation

The methane volume provided is an approximate value, including the water and tubing in the reactor. This measurement can have an error margin of ±5%, and the other values in the system are based on this methane volume.

Green Chemistry Assessment

This process demonstrates alignment with several principles of green chemistry:

- **Green oxidant**: Aqueous H_2O_2 decomposes into water and oxygen (clean, non-toxic byproducts).
- **Benign solvent**: Water is used as the sole reaction medium (no organic solvents).
- **Mild conditions**: 60 °C and moderate methane pressure (10 bar) in batch
- **High atom economy**: 92% for $CH_4 \rightarrow HCOOH$ transformation.
- **Low CO_2 formation**: Only 4–5% of carbon is lost as CO and CO_2.
- **One-step reaction**: Direct transformation of methane to formic acid without intermediates

- **Low precious metal loading:** Minimizes reliance on expensive and critical raw materials

The reaction was also successfully conducted under **continuous flow conditions** at **atmospheric pressure and 80 °C**. This mode of operation provides significant sustainability and process benefits:

- **Ambient pressure**: Safer and more energy-efficient than high-pressure batch systems.
- **Enhanced control**: Continuous flow improves heat and mass transfer, ensuring steady product formation.
- **Scalability**: Flow systems offer an easier transition to industrial-scale methane upgrading.
- **Catalyst compatibility**: The Au–Fe/Na-ZSM-5 catalyst maintained high activity and selectivity under flow.

The catalytic process offers a promising, sustainable route for methane valorization via selective oxidation to formic acid. It includes green solvents and oxidants, operates under mild and scalable conditions, and uses a low-metal-loading catalyst. These characteristics are consistent with the key principles of green chemistry and provide a strong basis for further development toward industrial application

References:

1 B. Ravel and M. Newville, *J Synchrotron Radiat*, 2005, **12**, 537–541.

2 B. Ravel, *J Synchrotron Radiat*, 2001, **8**, 314–316.

3 T. Yu, Z. Li, L. Lin, S. Chu, Y. Su, W. Song, A. Wang, B. M. Weckhuysen and W. Luo, *ACS Catal*, 2021, **11**, 6684–6691.

4 Z. K. Chu, G. Fu and X. Xu, in *Catalysis Today*, 2011, vol. 165, pp. 112–119.

5 J. Kučera and P. Nachtigall, *Physical Chemistry Chemical Physics*, 2003, **5**, 3311–3317.

6 T. Yu, Z. Li, W. Jones, Y. Liu, Q. He, W. Song, P. Du, B. Yang, H. An, D. M. Farmer, C. Qiu, A. Wang, B. M. Weckhuysen, A. M. Beale and W. Luo, *Chem. Sci.*, 2021, **12**, 3152–3160.

7 G. Qi, T. E. Davies, A. Nasrallah, M. A. Sainna, A. G. R. Howe, R. J. Lewis, M. Quesne, C. R. A. Catlow, D. J. Willock, Q. He, D. Bethell, M. J. Howard, B. A. Murrer, B. Harrison, C. J. Kiely, X. Zhao, F. Deng, J. Xu and G. J. Hutchings, *Nat Catal*, 2022, **5**, 45–54.

8 G. Kresse and J. Furthmüller, *Comput Mater Sci*, 1996, **6**, 15–50.

9 G. Kresse and J. Furthmüller, *Phys Rev B*, 1996, **54**, 11169–11186.

10 J. P. Perdew, K. Burke and M. Ernzerhof, *Phys Rev Lett*, 1996, **77**, 3865–3868.

11 M. Ernzerhof and G. E. Scuseria, *Journal of Chemical Physics*, 1999, **110**, 5029–5036.

12 A. Rohrbach, J. Hafner and G. Kresse, *Phys Rev B*, 2004, **70**, 125426.

13 S. Grimme, S. Ehrlich and L. Goerigk, *J Comput Chem*, 2011, **32**, 1456–1465.

14 D. Sheppard, R. Terrell and G. Henkelman, *Journal of Chemical Physics*, DOI:10.1063/1.2841941.

15 G. Henkelman, B. P. Uberuaga and H. Jónsson, *Journal of Chemical Physics*, 2000, **113**, 9901–9904.

16 H. J. Monkhorst and J. D. Pack, *Phys Rev B*, 1976, **13**, 5188–5192.

17 B. WOOD, *J Catal*, 2004, **225**, 300–306.

18 S. H. Choi, B. R. Wood, A. T. Bell, M. T. Janicke and K. C. Ott, *J Phys Chem B*, 2004, **108**, 8970–8975.

19 C. Hammond, M. M. Forde, M. H. Ab Rahim, A. Thetford, Q. He, R. L. Jenkins, N. Dimitratos, J. A. Lopez-Sanchez, N. F. Dummer, D. M. Murphy, A. F. Carley, S. H. Taylor, D. J. Willock, E. E. Stangland, J. Kang, H. Hagen, C. J. Kiely and G. J. Hutchings, *Angewandte Chemie International Edition*, 2012, **51**, 5129–5133.

20 C. Hammond, R. L. Jenkins, N. Dimitratos, J. A. Lopez-Sanchez, M. H. ab Rahim, M. M. Forde, A. Thetford, D. M. Murphy, H. Hagen, E. E. Stangland, J. M. Moulijn, S. H. Taylor, D. J. Willock and G. J. Hutchings, *Chemistry – A European Journal*, 2012, **18**, 15735–15745.

21 T. Yu, Z. Li, L. Lin, S. Chu, Y. Su, W. Song, A. Wang, B. M. Weckhuysen and W. Luo, *ACS Catal*, 2021, **11**, 6684–6691.

22 T. Yu, Z. Li, W. Jones, Y. Liu, Q. He, W. Song, P. Du, B. Yang, H. An, D. M. Farmer, C. Qiu, A. Wang, B. M. Weckhuysen, A. M. Beale and W. Luo, *Chem Sci*, 2021, **12**, 3152–3160.

23 E. J. M. Hensen, Q. Zhu, M. M. R. M. Hendrix, A. R. Overweg, P. J. Kooyman, M. V. Sychev and R. A. van Santen, *J Catal*, 2004, **221**, 560–574.

24 P. ROY and G. PIRNGRUBER, *J Catal*, 2004, **227**, 164–174.

25 Á. Szécsényi, G. Li, J. Gascon and E. A. Pidko, *ACS Catal*, 2018, **8**, 7961–7972.

26 G. Qi, T. E. Davies, A. Nasrallah, M. A. Sainna, A. G. R. Howe, R. J. Lewis, M. Quesne, C. R. A. Catlow, D. J. Willock, Q. He, D. Bethell, M. J. Howard, B. A. Murrer, B. Harrison, C. J. Kiely, X. Zhao, F. Deng, J. Xu and G. J. Hutchings, *Nat Catal*, 2022, **5**, 45–54.

27 S. S. Kanungo, A. K. Mishra, N. B. Mhamane, U. K. Marelli, D. Kumar and C. S. Gopinath, *Inorg Chem*, 2022, **61**, 19577–19587.

28 W. Huang, S. Zhang, Y. Tang, Y. Li, L. Nguyen, Y. Li, J. Shan, D. Xiao, R. Gagne, A. I. Frenkel and F. F. Tao, *Angewandte Chemie*, 2016, **128**, 13639–13643.

29 Z. Fang, H. Murayama, Q. Zhao, B. Liu, F. Jiang, Y. Xu, M. Tokunaga and X. Liu, *Catal Sci Technol*, 2019, **9**, 6946–6956.

30 K. Zhu, S. Liang, X. Cui, R. Huang, N. Wan, L. Hua, H. Li, H. Chen, Z. Zhao, G. Hou, M. Li, Q. Jiang, L. Yu and D. Deng, *Nano Energy*, 2021, **82**, 105718.

31 L. Lin, G. Zhang, L. Kang, T. Yu, Y. Su, G. Zeng, S. Chu and W. Luo, *ChemCatChem*, DOI:10.1002/cctc.202201234.